

# Directional Effects in a Daily AVHRR Land Surface Temperature Dataset Over Africa

Ana C. T. Pinheiro, Jeffrey L. Privette, Robert Mahoney, and Compton J. Tucker

**Abstract**—Land surface temperature (LST) is a key indicator of the land surface state and can provide information on surface-atmosphere heat and mass fluxes, vegetation water stress, and soil moisture. Split-window algorithms have been used with National Oceanic and Atmospheric Administration (NOAA) Advanced Very High Resolution Radiometer (AVHRR) data to estimate instantaneous LST for nearly 20 years. However, the low accuracy of LST retrievals associated with intractable variability has often hindered its wide use. In this study, we developed a six-year daily (day and night) NOAA-14 AVHRR LST dataset over continental Africa. By combining vegetation structural data available in the literature and a geometric optics model, we estimated the fractions of sunlit and shaded endmembers observed by AVHRR for each pixel of each overpass. Although our simplistic approach requires many assumptions (e.g., only four endmember types per scene), we demonstrate through correlation that some of the AVHRR LST variability can be attributed to angular effects imposed by AVHRR orbit and sensor characteristics, in combination with vegetation structure. These angular effects lead to systematic LST biases, including “hot spot” effects when no shadows are observed. For example, a woodland case showed that LST measurements within the “hot-spot” geometry were about 9 K higher than those at other geometries. We describe the general patterns of these biases as a function of tree cover fraction, season, and satellite drift (time past launch). In general, effects are most pronounced over relatively sparse canopies (tree cover <60%), at wet season sun-view angle geometries (principal plane viewing) and early in the satellite lifetime. These results suggest that noise in LST time series may be strongly reduced for some locations and years, and that long-term LST climate data records should be normalized to a single sun-view geometry, if possible. However, much work remains before these can be accomplished.

**Index Terms**—Angular effects, Advanced Very High Resolution Radiometer (AVHRR), geometric optics, land surface temperature (LST), vegetation structure.

## I. INTRODUCTION

**L**AND surface temperature (LST), defined as the effective kinetic temperature of the earth surface “skin,” is a key climatological variable and contributes to the magnitude and partitioning of energy fluxes at the earth’s surface. Knowledge of

the LST allows us to infer information about surface heat fluxes, vegetation properties, and soil moisture [1]–[3] and can help in the prediction of vegetation hydric stress and water requirements for crops [4], [5]. Currently, some model parameterizations [6] use air surface temperature to assess the surface state. However, LST is more directly related to surface properties than is the surface-level air temperature [7]. Therefore, improvement in the accuracy of LST retrievals would likely lead to more accurate parameterization of the surface. For example, Kustas and Norman [8] showed that uncertainty in LST of 1 °C to 3 °C could produce errors up to 100 W/m<sup>2</sup> in surface flux estimates.

Remote sensing is the only means available to monitor the temperature of the earth’s surface on a synoptic and regular basis. The National Oceanic and Atmospheric Administration (NOAA) Advanced Very High Resolution Radiometer (AVHRR) has measured the brightness temperature, a function of LST, of the earth for more than 20 years. However, orbit and sensor characteristics can impart temporal and spatial artifacts in the AVHRR data that impair their accuracy, especially as long-term time series. For example, the supposedly sun-synchronous orbit of the NOAA afternoon satellites drifts to later equatorial crossing times as the satellite ages. The drift has averaged approximately 30 min per year through their three- to five-year operational life [9]. For NOAA-14, this caused the local solar observation time, at the equator, to drift from 13:30 to later than 16:00. Recently, researchers have attempted to correct these effects [7], [10], [43] in some AVHRR products; however, no drift correction is currently applied to operational AVHRR LST products [e.g., NOAA, National Aeronautics and Space Administration (NASA)].

Effects of variability in the observation and illumination angles (i.e., sun-view geometry) on LST retrieval has received less attention. This variability results from two main factors: 1) the angular and local time variation across a single scan and 2) the nine-day periodicity of the AVHRR ground track. With a scan angle of  $\pm 55^\circ$  off nadir (equivalent to a  $68^\circ$  view zenith angle on the earth’s surface), the swath spans about 2 h in local time of observation at the equator. The time span increases with increasing latitude. The nine-day periodicity of the NOAA platform means that a given observation and illumination geometry associated with a given land target is only repeated each nine days.

For a flat Lambertian surface, the time of observation would be the primary cause of sensor-induced variability in the retrieved radiance. However, for a nonhomogeneous and structured surface, the sun-view geometry determines the relative proportions of the surface endmembers (e.g., sunlit soil, shaded trees) viewed by the sensor. Since endmember temperatures typically differ, the ensemble temperature of the scene can vary with the sun-view geometry.

Manuscript received September 4, 2003; revised March 13, 2004.

This project was funded in part by the PRAXIS Program (MCT, Portugal), in part by the Calouste Gulbenkian Foundation (Portugal), and in part by the National Aeronautics and Space Administration Goddard Space Flight Center. This project is part of the SAFARI 2000 Project.

A. C. T. Pinheiro was with the Biospheric Sciences Branch, NASA Goddard Space Flight Center, Greenbelt, MD 20771 USA. She is now with the Hydrological Science Branch, NASA Goddard Space Flight Center, Greenbelt, MD 20771 USA (e-mail: ana@hsb.gsfc.nasa.gov).

J. L. Privette and C. J. Tucker are with the NASA Goddard Space Flight Center, Greenbelt, MD 20771 USA.

R. Mahoney was with Global Science and Technology Incorporated, Greenbelt, MD 20771 USA. He is now with Northrop Grumman Corporation, El Segundo, CA 90245 USA.

Digital Object Identifier 10.1109/TGRS.2004.831886

In the past 20 years, many theoretical and empirical studies at local scale have addressed angular variability in thermal infrared measurements [11]–[13]. Further, some regional scale studies have exploited the dual-angle observations of the Along Track Scanning Radiometer (ATSR) to retrieve separate soil and vegetation temperatures [14], improve the estimates of surface sensible heat flux [15], and minimize errors in the retrieved sea surface temperature (SST) [16]. Several researchers [17]–[19] have speculated about the possible effects of sun-view geometry for global observations made with wide-field-of-view sensors. However, the effects have not been demonstrated for sensors with moderate spatial resolutions (i.e.,  $\geq 1$  km) such as AVHRR and Earth Observation System (EOS) Moderate Resolution Imaging Spectrometer (MODIS). The testing of this hypothesis can be challenging given the high-frequency changes in LST due to natural changes in meteorology (e.g., air temperature, cloudiness), surface conditions (e.g., soil moisture), and the natural diurnal cycle (solar heating). Indeed, this dynamic behavior is the desired signal from LST observations, and ideally should be significantly greater than observation-induced LST variability. If sun-view effects do exist, the LST data retrieved from AVHRR and MODIS would contain systematic variability imparted from sources independent of the natural land surface kinetic temperature.

In this paper, we describe a new daily NOAA-14 AVHRR LST dataset and interrogate it for evidence of angular variability over continental Africa. Specifically, we characterize systematic effects resulting from the varying observation and illumination geometry of AVHRR measurements in its nine-day periodicity as well as its six-year orbital decay.

In our approach, we assume that the most significant source of angular variability in the observed LST is a function of local vegetation structure and the temperatures of the endmembers, including shadows. To perform such a study at the continental scale, and for multiple years, many assumptions are required. We assume that each observation scene can be characterized by only four isothermal surface components (endmembers), and that directional differences in emissivity are negligible. This simplistic representation of surface temperature allows us to correlate LST to sun-view geometry given the projected fractions for those geometries.

## II. THEORY

The radiance reaching a thermal infrared (TIR) sensor, at height  $h$ , is the sum of two main components: the radiance emitted and reflected by the surface attenuated by the spectral transmittance of the atmosphere, and the upwelling radiance from the atmosphere integrated over the depth of the atmospheric path. The radiance detected by the sensor can be formulated as

$$L(\lambda, \theta, \phi, h) = \left( L(\lambda, \theta, \phi, 0) \tau_\lambda(\phi, \theta) + \int_0^h L(\lambda, T_{\text{at}}(z)) \frac{\partial \tau_\lambda(\phi, \theta, z)}{\partial z} dz \right) f(\lambda) \quad (1)$$

where  $f(\lambda)$  is the normalized response of the instrument in a finite bandpass,  $L(\lambda, T_{\text{at}}(z))$  is the upwelling thermal infrared

radiance (assumed isotropic) emitted by the atmosphere at height  $z$ ,  $\tau_\lambda(\phi, \theta, z)$  is the atmospheric transmittance at height  $z$ ,  $\tau_\lambda(\phi, \theta)$  is the total atmospheric transmittance along the path of observation, and  $L(\lambda, \theta, \phi, 0)$  is the radiance emitted by the surface and observed at zenith angles  $\theta$ , azimuth angles  $\phi$ , and at wavelength  $\lambda$ , and can be formulated as

$$\begin{aligned} L(\lambda, \theta, \phi, 0) &= B_\lambda[T_b(\theta, \phi)] \\ &= \varepsilon_\lambda(\theta, \phi) B_\lambda[T_{\text{sr}}(\theta, \phi)] + [1 - \varepsilon_\lambda(\theta, \phi)] (E_{\text{at}}/\pi) \end{aligned} \quad (2)$$

where  $T_b(\theta, \phi)$  is the surface directional brightness temperature, i.e., the temperature of a black body that has the same radiance as the radiance exiting that surface,  $\varepsilon_\lambda(\theta, \phi)$  is the directional emissivity of the surface, and  $E_{\text{at}}$  is the spectral irradiance at the earth's surface (assuming thermal equilibrium and a Lambertian atmosphere). Assuming knowledge of surface emissivity and irradiance, the directional radiometric temperature of the surface  $T_{\text{sr}}(\theta, \phi)$ , or apparent temperature of the surface, can be obtained by inverting Planck's function described as

$$B_\lambda[T_{\text{sr}}(\theta, \phi)] = \frac{2hc^2}{\lambda^5 (e^{hc/k\lambda T_{\text{sr}}(\theta, \phi)} - 1)} \quad (3)$$

with  $B[T_{\text{sr}}(\theta, \phi)]$  in units of watts per square meter per micrometer ( $\text{W} \cdot \text{m}^{-2} \cdot \mu\text{m}^{-1}$ ), and where  $h$  ( $6.6262\text{E-}34$  J·s) is the Planck constant,  $k$  ( $1.3806\text{E-}23$  J·K $^{-1}$ ) is the Boltzmann constant, and  $c$  ( $299\,792\,458$  m·s $^{-1}$ ) is the speed of light in the vacuum.

The radiometric temperature is also called the skin temperature [20], since it corresponds to the radiation emitted from a depth on the order of the penetration depth, i.e., on the order of the wavelength. The radiometric temperature (directional or hemispherical) is the best approximation of the surface thermodynamic temperature ( $T_s$ ) available from radiation measurements. The thermodynamic temperature, or kinetic temperature, is the “true” temperature of the surface and can be measured at a point with an accurate, infinitesimal *in situ* thermometer [21]. Radiometric and thermodynamic temperatures are the same only for homogeneous and isothermal surfaces—conditions that essentially never exist in nature.

For flat homogeneous surfaces, the variation of radiometric temperature retrieved by a radiometer, for different observation geometries, is mainly a function of the directional emissivity [12]. For structured and heterogeneous surfaces, the directional radiometric temperature is a function of the proportion of sampled area occupied by the different endmembers (hereafter referred to as “projected endmember fractions”) and their individual temperatures and emissivities (Fig. 1).

The temperatures of the soil and vegetation within a scene can be quite different depending on soil moisture, meteorological conditions, exposure to sunlight, as well as the time of observation. [22] observed temperature differences between soil and soybean canopy of up to 11 °C. Higher values ( $>20$  °C) were observed by [23] using a mobile scanner over a savanna in Botswana and over a vineyard in Central Spain. It is, therefore, not surprising that experimental studies provide evidence of large angular variations in apparent temperature for vegetated surfaces. For example, Kimes and Kirchner [24] observed differences of 16.2 °C in radiative temperature between 0° and 80° view zenith angle for measurements taken over a cotton field at noon.

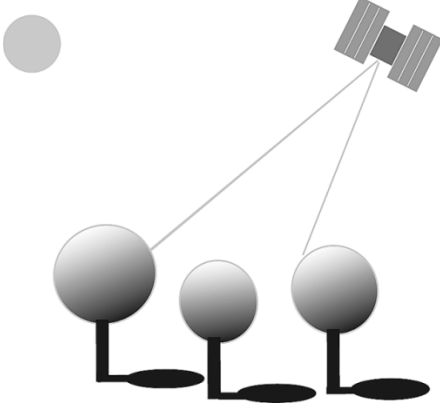


Fig. 1. Schematic representation of scene endmembers.

### A. Modeling the Apparent Temperature

The variability of radiometric temperature due to sun-view geometry can be characterized using a physically based mathematical model. Geometric projection models [24]–[26] determine the projected endmember fractions ( $X_{k,\theta,\phi}$ ), i.e., the proportions of the different endmembers as projected on the plane perpendicular to the direction  $(\theta, \phi)$  of observation. The sum of all projected fractions equals unity. Geometric models represent the vegetation as opaque solids (no within canopy gaps) and do not simulate the radiative transfer within the canopy. The endmembers can include the sunlit and shaded areas of crown and soil and are used to weight the radiances emitted by each isothermal endmember.

To estimate the ensemble temperature of a surface, let us consider a large area, with a spatial extent on the order of a satellite observation, composed of  $N$  homogeneous endmembers each of which is characterized by a temperature  $T_k$ , emissivity  $\varepsilon_k$ , and fractional cover  $X_{k,\theta,\phi}$ .

We will assume that the radiance emitted from the target scene is a linear contribution of the radiances emitted by each endmember weighted by its projected fraction. Moreover, we will assume that endmembers are isotropic reflectors and emitters and that any variation in the scene-emitted radiance depends on the variation of the projected fractions only, i.e.,

$$\langle L(\lambda, \theta, \phi, h) \rangle = \sum_{k=1}^N L(\lambda, \theta, \phi, h)_k X_{k,\theta,\phi} \quad (4)$$

where  $\langle L(\lambda, \theta, \phi, h) \rangle$  is the scene radiance emitted for wavelength  $\lambda$ , and  $L(\lambda, \theta, \phi, h)_k$  is the radiance emitted by endmember  $k$ . The scene radiative temperature  $\langle T_{\text{sf}} \rangle$  can be estimated as

$$\langle T_{\text{sf}} \rangle = \left[ \frac{1}{\langle \varepsilon \rangle} \sum_{k=1}^N \varepsilon_k T_{\text{sk}}^4 X_{k,\theta,\phi} \right]^{1/4} \quad (5)$$

with  $\langle \varepsilon \rangle$  defined as the weighted mean of endmember emissivities, i.e.,

$$\langle \varepsilon(\lambda, \theta, \phi) \rangle = \sum_{k=1}^N \varepsilon_k(\lambda, \theta, \phi) X_{k,\theta,\phi}. \quad (6)$$

For the AVHRR bands between 10–12  $\mu\text{m}$ , Becker and Li [21] demonstrated that  $\langle T_{\text{sf}} \rangle$  and  $\langle T_{\text{sr}} \rangle$  are very similar.

In this study, we consider scenes with discontinuous canopies composed of four endmembers: sunlit crown, shaded crown, sunlit background, and shaded background. The projected fractions  $X_{k,\theta,\phi}$  are modeled using the geometric optics bidirectional reflectance (GORT) model [27]. The GORT model was developed to estimate the bidirectional reflectance distribution function (BRDF) of plant canopies. Here we will use only the geometric optics (GO) component of the model. The GO model simulates a scene of discontinuous canopies as a collection of spheroids on vertical sticks. The location of those spheroids follows a Poisson distribution. The model uses Boolean set theory to calculate within and between crown gap probabilities. As input, it requires specification of tree crown center height (minimum and maximum), crown radius (horizontal and vertical), and fractional tree cover. The results allow estimation of the four endmembers. For more information, readers may consult [27].

## III. DATA

### A. Vegetation Structure for Africa

To apply the GO model over Africa, we need maps of vegetation structure and AVHRR sensor observation and illumination geometries. As we were unaware of any digital maps of vegetation structure for continental Africa in the literature, we created maps [28] based on the land cover map developed in [29] (hereafter called “UMD land cover map”) and ancillary vegetation information compiled by White [30]. Additionally, we used the continuous fields maps for woody, herbaceous, and barren cover described in [31]. This latter product quantifies, on a pixel basis, the percent cover of woody material, herbaceous material, and bare soil and will be hereafter referred as “UMD continuous fields.”

We associated the vegetation structural characteristics from White to the respective UMD map units and generated four maps corresponding to the following:

- 1) maximum tree height;
- 2) minimum tree height;
- 3) average crown horizontal diameter;
- 4) average crown vertical diameter.

The largest uncertainty in these maps is in the crown shape (diameter and height), since limited information is available from White for most of the phytochoria. Where no structural information was available, we assigned the characteristics for another area having a similar description. We applied a land/water mask to our maps and then used bilinear interpolation to fill the gaps with missing data.

We performed a sensitivity study [32] that revealed that the GO model is most sensitive to the tree fractional cover and is minimally sensitive to minimum tree height, maximum tree height, and vertical crown radius. The model also showed low sensitivity to horizontal crown radius where the overall percent tree cover remains fixed.

### B. AVHRR Land Surface Temperature

We created an LST dataset based on NOAA-14 AVHRR/2 Global Area Coverage (GAC; 4-km resolution) data within the

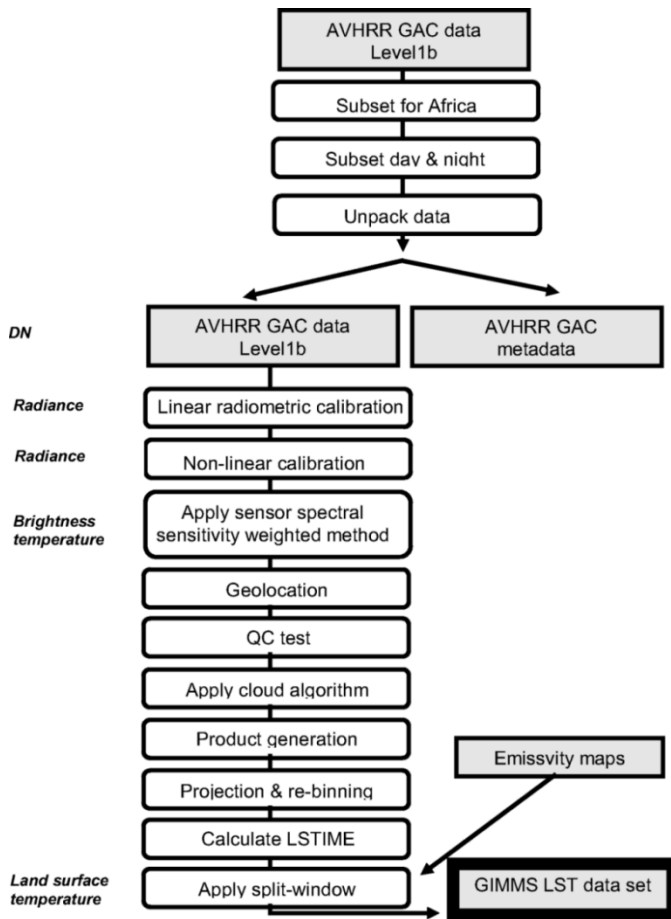


Fig. 2. Schematic representation of NOAA-14 AVHRR LST product processing chain in NASA's GIMMS.

Global Inventory Mapping and Monitoring System (GIMMS). The product was generated for each day and night pass and over the full swath width of the AVHRR scan ( $\pm 55^\circ$ ).

The GAC data were obtained from the NOAA Satellite Active Archive (<http://www.saa.noaa.gov>) in level-1b format. We processed these data using a modified version of the global area processing system [33]. We processed the daily orbits over the operational lifetime of NOAA-14 (1995 to 2000). Fig. 2 shows a schematic representation of the steps used to process the AVHRR brightness temperature data (channel 3, channel 4, and channel 5, with central wavelength at 3.74, 10.8, and 12  $\mu\text{m}$ , respectively) and the collateral products (e.g., observational angles, illumination angles, and local solar time of overpass).

One of the initial steps involved radiometric calibration, i.e., converting the digital counts to radiance in milliwatts per square meter per steradian per centimeter [ $\text{mW}/(\text{m}^2 \cdot \text{sr} \cdot \text{cm})$ ], followed by a nonlinear calibration of channels 4 and 5, to account for nonlinear response of the detectors to incoming radiance. The radiance was then converted to brightness temperature using the spectral response functions and assuming that the earth emits as a blackbody in the spectral wavelengths of interest.

Quality control flags produced in the previous steps were analyzed so that pixels with faulty or missing data were identified. We applied the CLAVR-1 cloud algorithm [34] to identify fully and partially cloudy pixels.

The products were mapped into Albers equal area projection and simultaneously rebinned to 8 km  $\times$  8 km pixel size to be compatible with the GIMMS NDVI dataset [33]. We rebinned using forward mapping and selecting the maximum brightness temperature in channel 5 (T<sub>5</sub>). A map of the observation local solar time (LSTIME) was also produced.

The brightness temperatures retrieved in the AVHRR thermal bands (channels 4 and 5) correspond to top-of-atmosphere (TOA) brightness temperatures, i.e., not atmospherically corrected. To derive LST, we applied a split-window technique. The method takes advantage of differential absorption in two spectrally close infrared bands to account for the effects of absorption and emission by atmospheric gases. For the AVHRR thermal infrared bands, atmospheric attenuation is greater in channel 5 than in channel 4. This difference increases for increasing water vapor. Since surface emission is assumed to differ negligibly between the bands, the differential shift in sensor measured radiance results almost entirely from atmospheric attenuation.

We implemented the Ulivieri [35] split-window algorithm, i.e.,

$$T = T_4 + 1.8(T_4 - T_5) + 48(1 - \varepsilon) - 75\Delta\varepsilon \quad (7)$$

where  $T_4$  and  $T_5$  are the brightness temperatures (in kelvin) of AVHRR channels 4 and 5, respectively, and

$$\varepsilon = (\varepsilon_4 + \varepsilon_5)/2 \quad (8)$$

$$\Delta\varepsilon = \varepsilon_4 - \varepsilon_5. \quad (9)$$

Equation (7) was developed for cases of column atmospheric water vapor less than 3.0 g/cm<sup>2</sup>, a reasonable condition for much of the semiarid portions of continental Africa. Becker and Li [21] tested the Ulivieri algorithm using four different datasets as part of an intercomparison between seven different LST split-window algorithms. In all cases, the Ulivieri algorithm performed well. The authors note, however, that for the small range of water vapor content exhibited by the datasets used, it is not possible to fully access the effectiveness of the split-window algorithms. A later algorithm comparison [36] yielded similar results, and indicated that the Ulivieri algorithm was least dependent on accurate knowledge of surface emissivity. This is beneficial, since there are no validated emissivity maps of continental Africa.

To estimate  $\varepsilon_4$  and  $\varepsilon_5$ , we developed static emissivity maps following an approach similar to [37] based on landcover and soil classification maps [29]. We determined the soil types from the Food and Agriculture Organization (FAO) Soil Map of Africa [38]. We assigned an emissivity value for each (Table I) based on the spectral emissivity data from the Jet Propulsion Laboratory (JPL) (<http://speclib.jpl.nasa.gov/>) convolved with the AVHRR spectral response functions.

We generated two maps of emissivities for vegetated areas: one for tree cover emissivity and another for herbaceous cover emissivity. Again, the emissivity values for the appropriate vegetation classes were obtained by convolving the JPL spectral emissivities with the spectral response functions.

We assumed the scene directional emissivity is primarily determined by the variability in the projected endmember fractions, where the shaded and sunlit components of a given

TABLE I  
AVERAGE EMISSIVITIES FOR AVHRR CHANNELS 4 AND 5 ASSIGNED TO EACH FAO SOIL CLASS AND VEGETATION TYPE

FAO SOIL CLASS	EMISSIVITY	
	Channel 4	Channel 5
Mollisols	0.973	0.978
Vertisols	0.973	0.980
Ultisols	0.961	0.975
Inceptisols	0.970	0.974
Alfisols	0.969	0.976
Entisols	0.973	0.980
Solonchaks	0.975	0.975
Aridisols	0.969	0.974
Oxisols	0.977	0.976
Spodosols	0.970	0.971
Histosols	0.973	0.978
Rock and Rockland (granite/basalt)	0.954 / 0.977	0.940 / 0.968
Salt	0.975	0.975
Water	0.994	0.986

UMD LAND COVER TYPE (CLASS)	EMISSIVITY	
	Channel 4	Channel 5
Evergreen forest (1, 2)	0.989	0.991
Deciduous forest (3, 4)	0.974	0.973
Mixed forest (5), Woodland (6), Wooded grassland (7), Closed shrubland (8), and Open shrubland (9)	0.982*	0.982*
Grassland (10), agricultural (11)	0.982	0.989

\* 50% evergreen and 50% deciduous.

Note 1: no data available for oxisols class. We adopted the emissivity for alfisols class which has similar physical description in the epipedon.

Note 2: default rockland is granite with exception of soils in Kenya: basalt.

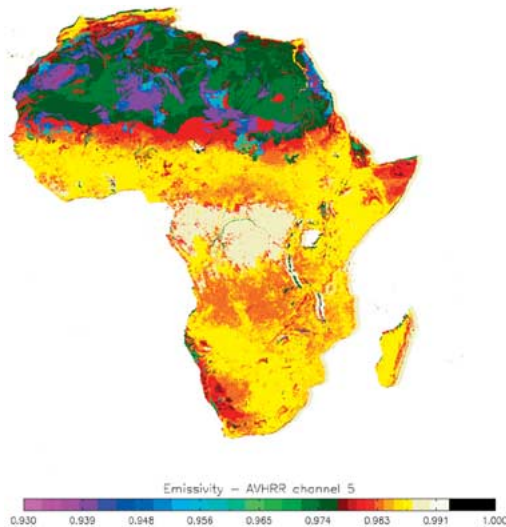


Fig. 3. Emissivity map for AVHRR channel 5.

endmember share a common emissivity value. Using the endmember emissivity maps and (6), we calculated the scene emissivity for each pixel (Fig. 3) by weighting the endmembers emissivities by their cover fraction based on the UMD continuous fields estimates for woody cover, bare soil cover, and herbaceous cover.

#### IV. METHODS AND RESULTS

##### A. AVHRR Geometry Variability Over Africa

We initially sought to assess the sun-view effects on projected fractions and LST. Our first step was to characterize the sun-

view geometries both seasonally and annually. Specifically, we created continental maps of solar and view zenith angles and the relative azimuth angles for the equinox and solstice dates from 1995 to 2000.

1) *Seasonal Effects*: Composite maps (i.e., depicting all satellite overpasses within a day) of the relative azimuth angle are shown in Fig. 4. The AVHRR ground track, where view zenith angle is zero (nadir), is identified by the linear southeast-to-northwest trending lines in each map. The highly fractured line parallel to the ground track represents areas where AVHRR sampling overlaps on consecutive orbits (edge- of-scan) and results from compositing for maximum brightness temperature in channel 5, for consecutive orbits. The maps are color coded to indicate subranges of relative azimuth angle as shown in the color bar.

The most notable aspects of Fig. 4 include the alignment of the solar principal plane (lighter colors where the relative azimuth angle is close to  $0^\circ$  or to  $180^\circ$ ) with the AVHRR scan direction (i.e., perpendicular to the ground track) at certain latitudes, and the variable alignment of “iso-azimuth angles” (constant colors) relative to the AVHRR scan direction within a season. First, the AVHRR scans directly along the principal plane in northern Africa in June (around summer solstice), near the equator in March and September (around equinoxes), and in southern Africa in December (around winter solstice). Previous studies (e.g., [32] and [39]) have demonstrated that the projected endmember fractions change most along the principal plane. Combined, these results suggest that the AVHRR experiences “worst case” geometric conditions at different locations in Africa throughout the year. Conversely, the AVHRR essentially scans along the perpendicular plane (i.e., across azimuth angles) in the opposing hemisphere: the

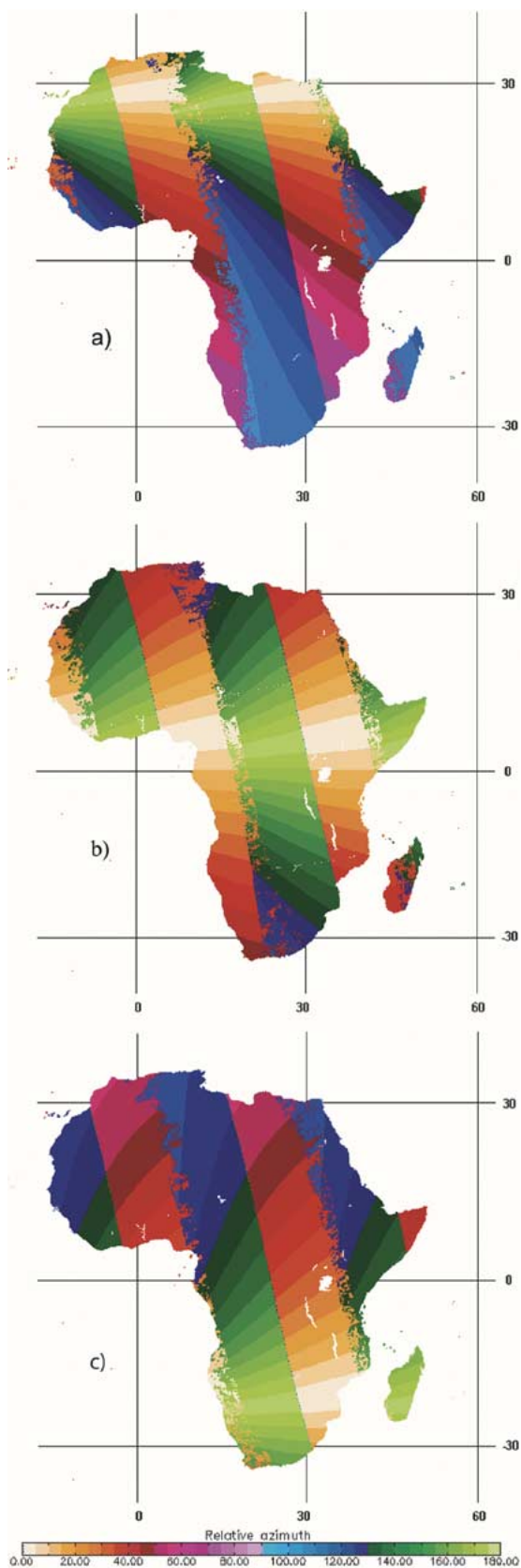


Fig. 4. Continental maps of relative azimuth angle between AVHRR observation and solar incidence directions for year 1995 for (a) summer solstice (June), (b) equinox (March and September), and (c) winter solstice (December). Lighter colors indicate where the relative azimuth angle is close to  $0^\circ$  or  $180^\circ$  (i.e., solar principal plane). The northwest trending lines correspond to the satellite ground tracks.

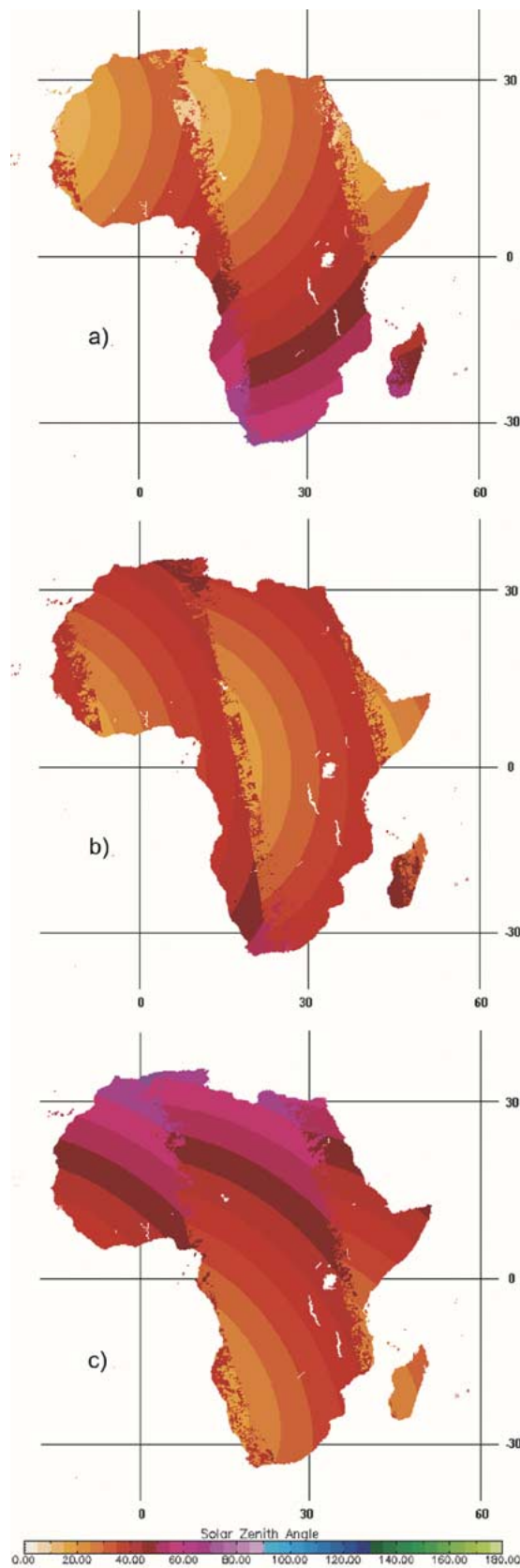


Fig. 5. Continental maps of solar zenith angle for AVHRR observations in year 1995 for (a) summer solstice (June), (b) equinox (March and September), and (c) winter solstice (December).



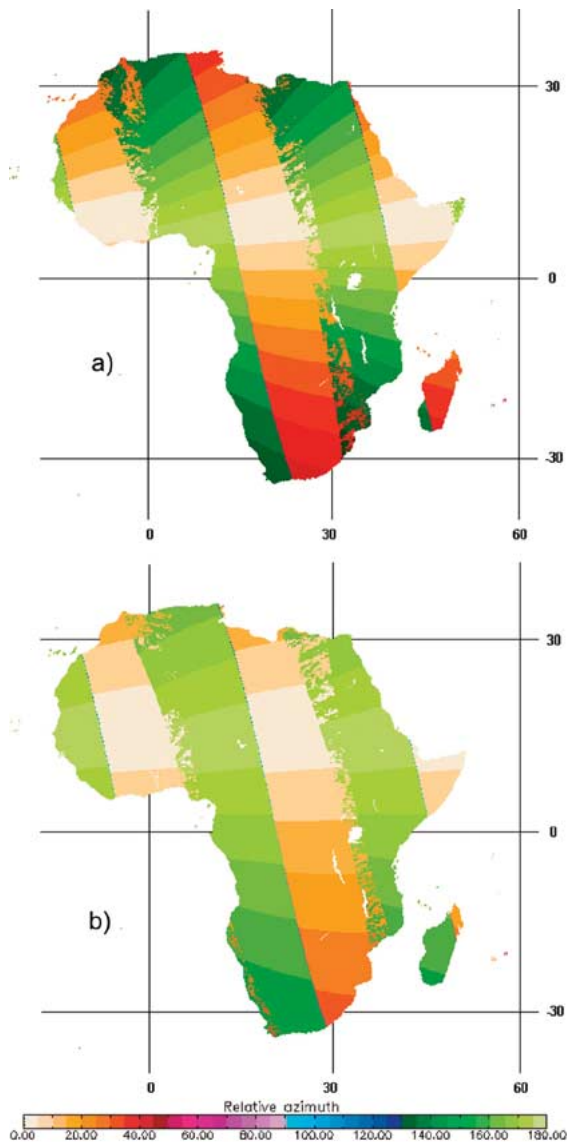


Fig. 6. Maps of relative azimuth angle between AVHRR and solar directions at equinoxes for years (a) 1998 and (b) 2000.

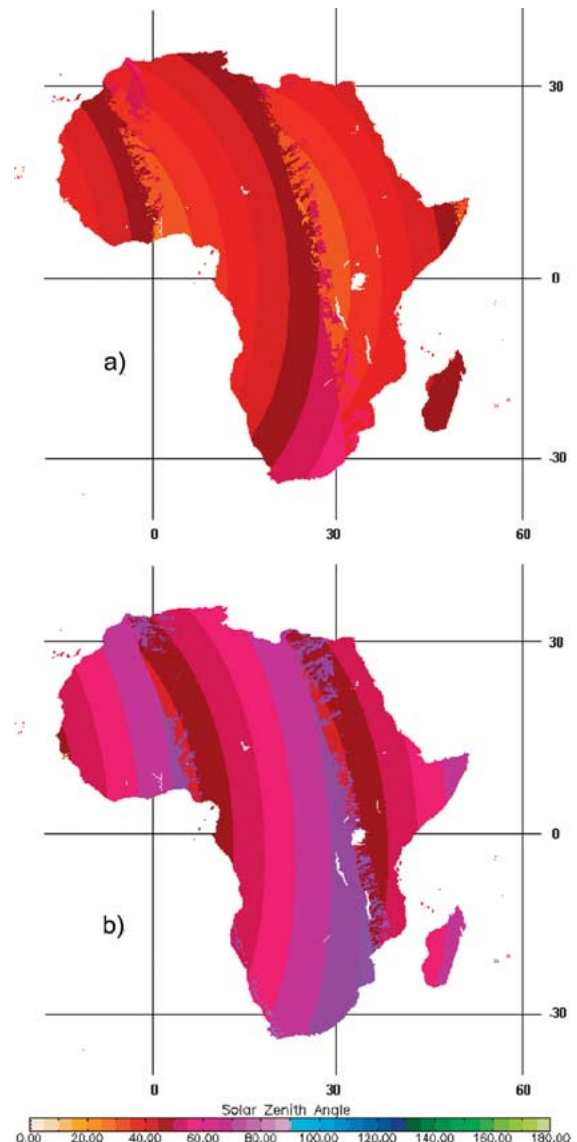


Fig. 7. Maps of solar zenith angle between AVHRR and solar directions at equinoxes for years (a) 1998 and (b) 2000.

south in June and north in December. Because the projected endmember fractions vary less and are symmetric about nadir in the perpendicular plane, this provides a “best case” sampling scenario where little LST sun-view geometry bias would be expected.

The solar zenith angle (SZA) maps (Fig. 5) show a concentric circular pattern as would be expected for the sun-synchronous NOAA-14 orbit. Although the NOAA ground track is not visible, the fractured line corresponding to the overlapping areas on consecutive orbits is visible. The maps illustrate the very large solar zenith angle range ( $0^\circ$  to  $70^\circ$  during solstices) over which AVHRR samples along a given longitude, for a near-constant local time. In the north in June, an AVHRR swath may span a range from  $0^\circ < \text{SZA} < 40^\circ$ , but in the south a swath spans a very limited range (e.g.,  $50 < \text{SZA} < 55$ ). This means that near constant illumination conditions exist for the pixels along a scan in the south hemisphere, but very different illumination conditions occur along a scan in the north hemisphere. The opposite is true in December. This complicates the determination

of LST in principal plane sampling. In addition, a step-function bias may occur where consecutive scans overlap, since solar angle changes of up to  $40^\circ$  can exist among adjacent pixels if sampled on different orbits.

2) *Drift Effects:* As noted above, the NOAA-14 orbit drifts to later afternoon equator crossing times as the satellite ages. This drift rate accelerates over time. The impact of drift on the relative azimuth angles of AVHRR is obvious by comparing year 1995 [Fig. 4(a)] with year 2000 [Fig. 6(b)]. In the latter case, the azimuth angles from all points on the continent converge toward the principal plane. The AVHRR is, therefore, sampling at azimuth angles most vulnerable to sun-view angle effects during both the wet and dry season regions. Solar angle maps (Fig. 7) illustrate the increasing solar zenith angles in later years. By 2000 [Fig. 7(b)], the iso-angle regions are nearly parallel to the AVHRR ground track over the continent, indicating that the AVHRR scan always sweeps across a large range ( $45^\circ < \text{SZA} < 80^\circ$ ). This could suggest high variability in projected endmember fractions. In a later section, we will

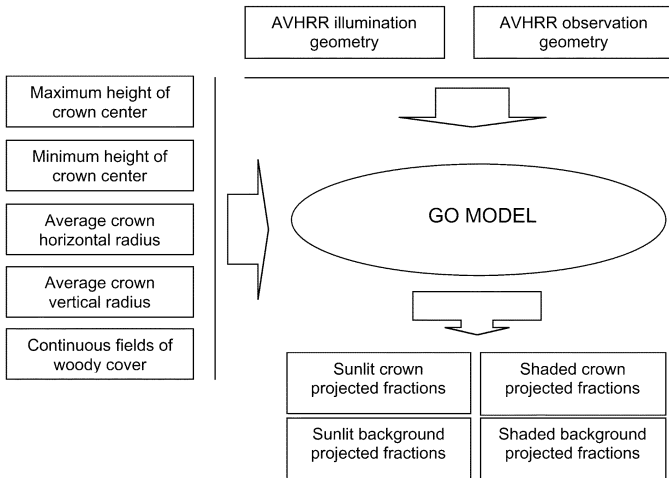


Fig. 8. Schematic representation of modeling approach used for each pixel and AVHRR orbit using a GO model.

see how temperature changes with time can mitigate this effect.

In sum, the geometric characteristics alone suggest that LST biases could be greatest in the regions experiencing the wet season at a given time, and that the area experiencing strongest effects increases as the satellite drifts.

### B. Simulations of Structural Impacts in LST

Based on the vegetation structural maps described in Section III-A, we parameterized the GO model for each pixel of continental Africa and Madagascar. Since the GO model requires the maximum and minimum heights of crown center, we assumed

$$\text{maximum\_height\_crown\_center} = \text{maximum\_tree\_height} \times 2/3 \quad (10)$$

$$\text{minimum\_height\_crown\_center} = \text{minimum\_tree\_height} \times 1/3. \quad (11)$$

For each AVHRR orbit and pixel, we used the GO model to estimate the endmember fractions projected into the AVHRR observation direction. We combined them to create four composite fraction maps: sunlit crown, shadowed crown, sunlit background, and shadowed background. A schematic representation of the process is shown in Fig. 8.

The maps in Fig. 9 illustrate the day-to-day variability in scene endmembers visible to AVHRR. For example, Fig. 9(a) and (c) shows the sunlit crown and background projected fractions, respectively, for the sampling conditions on day of year (DOY) 71 (March 11) of year 2000. To help discriminate the effects of vegetation characteristics from those of sun-view geometry, we compared the projected fractions for DOY 71 and 75 (March 15) in Fig. 9(b) and (d). Although these dates are just four days apart, differences in the projected fractions are visible—especially over Angola and Zambia (between 5° and 15° south of the equator) where the sunlit crown changes, between dates, from more than 50% to less than 40%. This variation is due strictly to sun-view geometry differences.

Because projected fractions vary with sun-view geometry, land cover type and tree cover percentage, it is difficult to isolate

features imparted by individual sources. Nevertheless, a gradient coinciding with view zenith angles is visible in Fig. 9(b) over the Congo forest region (from approximately 5° north of the equator to 7° south of the equator).

To assess the impact of projected fractions on AVHRR LST, we simulated the scene temperatures for the same dates. We assigned a fixed temperature to each of the four endmembers (Table II) to represent typical midday conditions for a semi-arid African environment. Specifically, sunlit background is the hottest endmember, and is 13° warmer than the shaded background. Sunlit and shaded crown differ by just 2° and are of similar temperature to the shaded background. We calculated the scene temperatures based on the projected fractions for DOY 71 and 75 using (5) and assuming that endmembers behave as blackbodies. To facilitate comparison, we created a map of the LST difference between the days ( $\Delta T$ ).

As shown in Fig. 10, the differences in temperature ( $-5 < \Delta T < 5$ ) are generally parallel to the AVHRR ground tracks (southeast to northwest). The greatest changes occur where targets were sampled in the solar backscatter region of the principal plane on one date and the forward scatter region of that plane on the other date. To the right (east) of the ground track, there is a positive bias due to the decrease of shadows viewed by the sensor in the solar backscatter region. Conversely, there is a negative temperature bias for pixels to the left (west) of the ground track due to increase in shadow visible in the solar forward scatter region. Since shaded components are cooler than sunlit components, the scene radiance in the forward scatter direction is always less than that in the backward direction. This demonstrates the impacts of shadow endmember variability.

Further, there is an obvious variation with overstory cover. For example, relatively small differences are observed over the Congo forest region where the crown density is high (approximately 80% tree cover). In this case, the understory is minimally visible to the AVHRR, and the main contributors to the scene radiance are sunlit crown and shadowed crown. Finally, for this time of year, variability is stronger north of the equator over sparsely vegetated surfaces (woodlands and wooded grasslands) where observations are made closer to the principal plane [recall Fig. 4(b)].

### C. View Angle Effects on AVHRR LST

The six-year daily AVHRR dataset described above is sufficiently voluminous that full characterization is not possible here. Instead, we provide a series of “tell-tale” examples that typify its inherent directional effects. Given the demonstrated dependency of the projected fractions on the surface vegetation structure, we stratified our analysis into two categories: 1) sparse and 2) dense tree cover.

In the first category (sparse), we included two land cover types: woodland and wooded grassland. In the second category (dense), we include the forest land cover type only. Note that tree cover data are not available for the open shrubland and closed shrubland classes [30], and therefore, those areas are not considered in our study.

1) *Sparse Tree Cover*: For sparse covers, we first analyzed the areas that showed high angular sensitivity in our simulations (i.e., Fig. 10). We plotted the true AVHRR LST versus



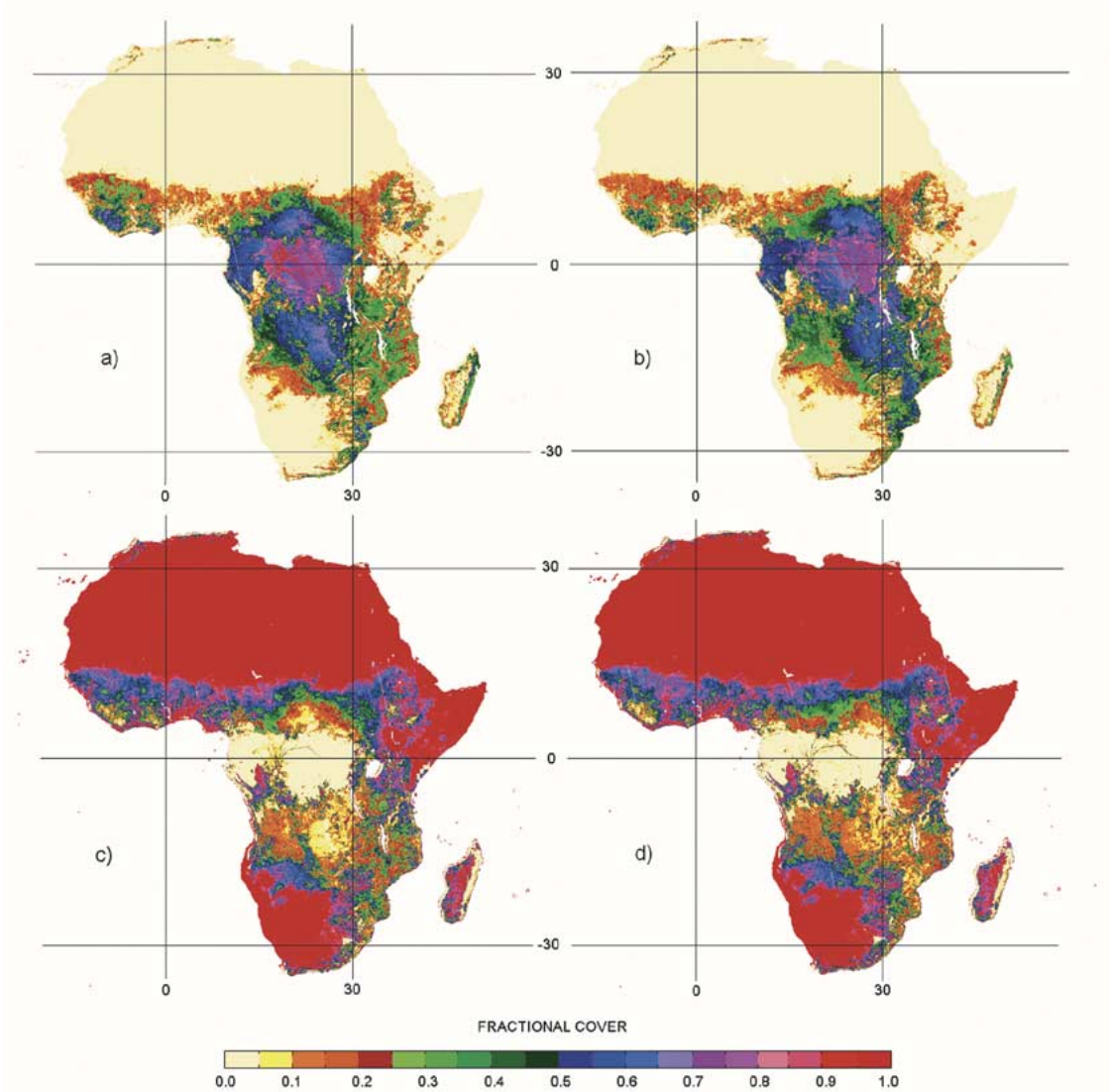


Fig. 9. Sunlit crown projected fractions as viewed by the AVHRR NOAA-14, on (a) DOY 711998 and (b) DOY 75 1998. Background projected fractions as viewed by the AVHRR NOAA-14 on (c) DOY 711998 and (d) DOY 751998.

TABLE II  
TEMPERATURES ASSIGNED TO ENDMEMBERS FOR SIMULATION

Endmember	Endmember symbol	Temperature function	Temperature value (K)
Sunlite canopy	$T_{cs}$	fixed	295
Delta-temperature-canopy	$\Delta T_c$	fixed	2
Shaded canopy	$T_{csh}$	$T_{cs} - \Delta T_c$	293
Sunlite background	$T_{bs}$	fixed	305
Delta-temperature-background	$(T_b)$	fixed	13
Shaded background	$T_{bsh}$	$T_{bs} - (T_b)$	292

the view zenith angle (with positive angles for forward observations) for a window of  $30 \times 30$  pixels centered at latitude  $\approx 7^\circ$  and longitude  $\approx 24^\circ$  (i.e., the greatest negative bias in simulation). We selected pixels with the same land cover type (woodland) and used data for 16 days, or two orbital cycles of the AVHRR, to ensure that we covered the full range of AVHRR geometries. Although there is natural LST variability in 16 days, we assumed this variability was not excessive and would not mask biases due to sun-view geometry.

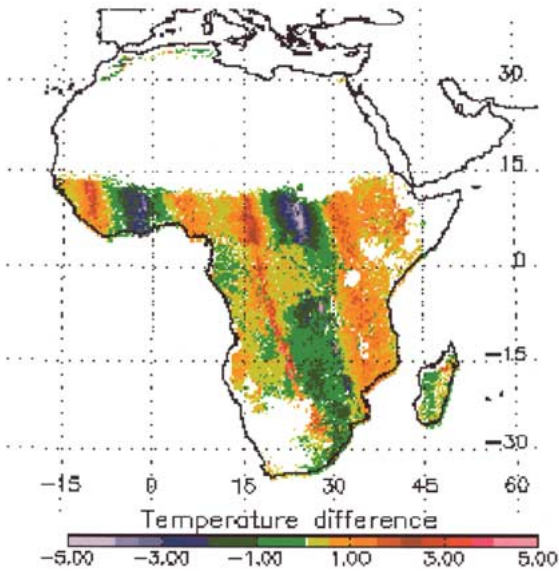


Fig. 10. Differences in simulated temperature observed by NOAA-14 AVHRR between DOY 711998 and 751998, due strictly to sun-target-sensor geometry.

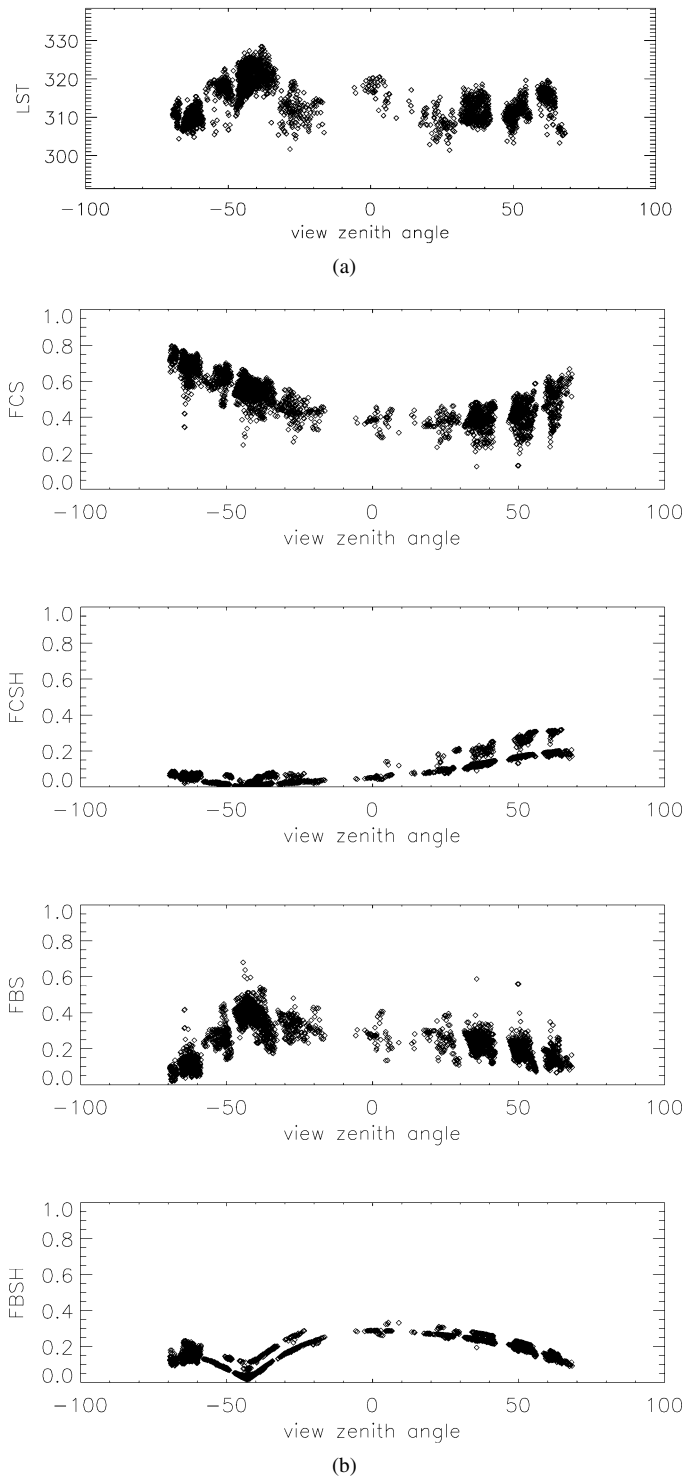


Fig. 11. (a) AVHRR LST (in kelvins) as a function of view zenith angle (degrees), for AVHRR measurements taken around the vernal equinox (1998) over the woodland study area. (b) Sunlit canopy (FCS), shaded canopy (FCSH), sunlit background (FBS), and shaded background (FBSH) projected fractions (percent) as a function of view zenith angle (degrees), for AVHRR measurements taken around the vernal equinox (1998) over the woodland study area.

The variability of LST with view zenith angle during the 1998 vernal equinox is shown in Fig. 11(a). The associated relationships between the projected fractions and the view zenith angle [Fig. 11(b)] suggest that the LST closely follows the trend of the projected sunlit background fraction (FBS). For such a moderate tree cover (average = 45%), this correlation is logical,

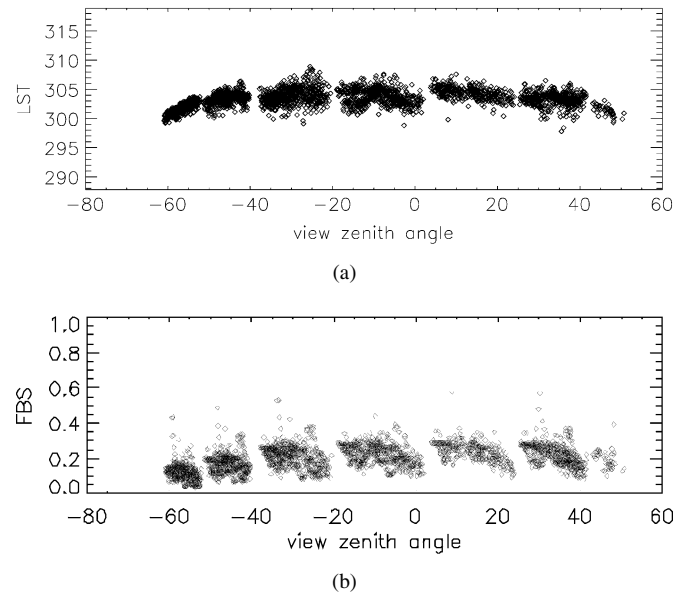


Fig. 12. (a) AVHRR LST (in kelvins) as a function of view zenith angle (degrees), for AVHRR measurements taken around the vernal equinox (2000) over the woodland study area. (b) Sunlit background (FBS) projected fraction (percent) as a function of view zenith angle (degrees), for AVHRR measurements taken around the vernal equinox (1998) over the woodland study area.

since the sunlit background endmember is typically warmest [22] at the time of AVHRR overpass (between 13:30 and 15:30) along a swath for this particular year. The correlation between these two parameters is  $r = 0.64$ , indicating that 41% of the total variability of LST can be explained alone by the fraction of sunlit background observed by the AVHRR. Note that a range of projected fractions exists for a given view zenith angle due to the inclusion of pixels with different tree cover fractions in the  $30 \times 30$  pixels window.

We also observe a hot spot around  $-40^\circ$  view zenith angle, since the solar zenith angle for those observations is about  $40^\circ$ , and the relative azimuth angles are close to  $0^\circ$ . The primary cause of the hotspot is the absence of shadows when the viewing direction coincides with the illumination direction. Although "hot spot" evolves from bidirectional reflectance research, it is appropriate here, since it represents the view geometry of maximum scene temperature for a given target at a given time.

If we consider a different season, e.g., for the summer solstice, the configuration required for the hot spot no longer occurs at the same location. Indeed, Fig. 12(a) and (b) confirms the absence of the hot spot but still shows that the LST pattern with view zenith angle most closely follows the projected fraction of sunlit background.

2) *Dense Tree Cover*: If we apply our window to densely vegetated regions, we find different patterns. Fig. 13(a) shows the relationship between AVHRR LST and view zenith angle for a forest (mean tree cover = 83%), centered at latitude  $\approx 2^\circ$  south and longitude  $\approx 22^\circ$  East, during the vernal equinox of 1995. Note that cloud contamination limited the number of pixels available for this analysis. In this case, LST is most closely correlated with sunlit crown cover [Fig. 13(b)]. With more complete overstory canopy coverage (compared to the sparse case), the contribution of the background is negligible relative to that of the crowns.

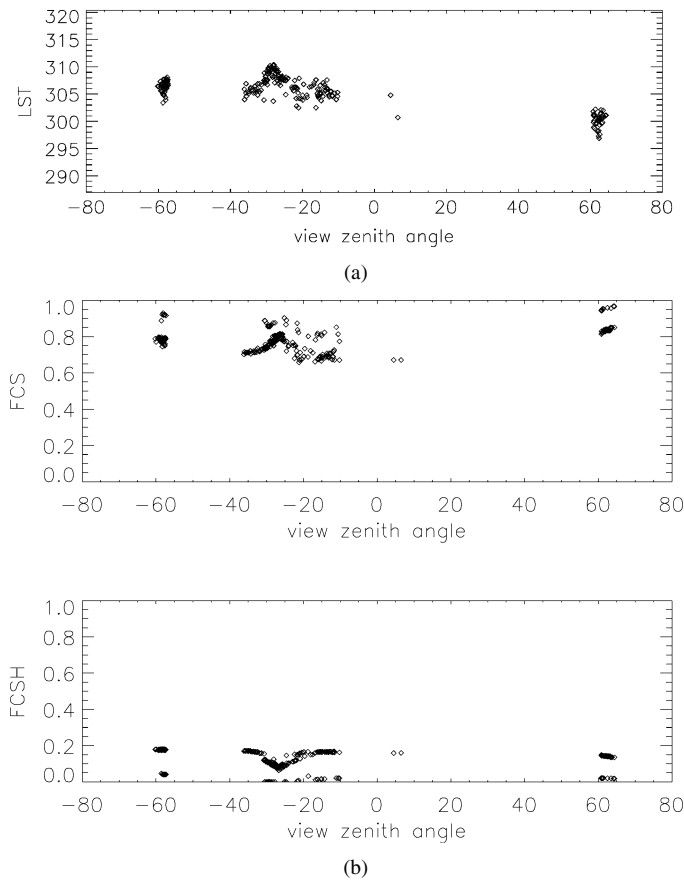


Fig. 13. (a) AVHRR LST (in kelvins) as a function of view zenith angle, for AVHRR measurements taken around the vernal equinox (1995) over the forest study area. (b) Sunlit canopy (FCS), and shaded canopy (FCSH) projected fractions (percent) as a function of view zenith angle, for AVHRR measurements taken around the vernal equinox (1995) over the forest study area.

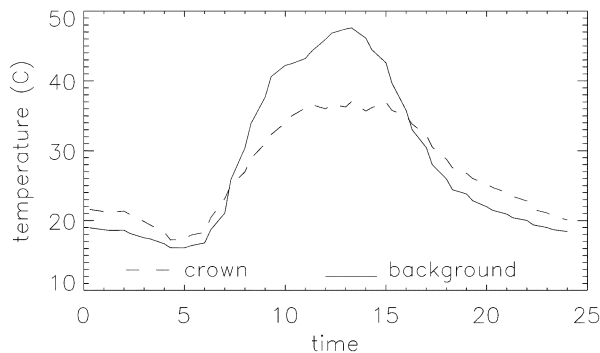


Fig. 14. Tree crown and background endmember radiometric temperatures for a savanna near Skukuza, South Africa on day 272 of year 2000. Note time of NOAA-14 overpass for years 1995 and 2000.

#### D. Orbital Drift Effects on AVHRR LST

Before discussing the scene-level temperature trends, it is instructive to consider the typical daily behavior of individual endmember temperatures for a savanna site in eastern South Africa (Fig. 14; tree cover = 31%, tree crown height = 9 m). In this example, only the tree crown and background are represented. The data show that for clear sky conditions, the background temperature rapidly outpaces the sunlit crown temperature after about 08:30 hours in response to morning irradiance. The peak

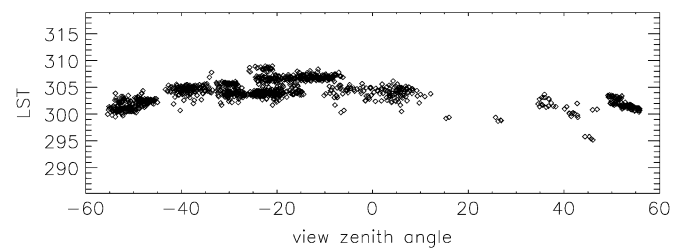


Fig. 15. AVHRR LST (in kelvins) as a function of view zenith angle (degrees), for AVHRR measurements taken around the vernal equinox (2000) over the forest study area.

difference occurs near 13:00 hours, after which time the temperatures begin to converge. By about 16:30 hours, the crown and background temperatures are equal, and toward sunset (~17:00 hours), the crown temperature begins to exceed the background temperature. We will refer back to this example in our analysis of orbital drift below.

To assess the impacts of orbital drift, we considered the extreme geometry conditions of the year 2000. As shown before, NOAA-14 AVHRR increasingly samples points near the principal plane as time past launch increases. Since directional effects are greatest in the principal plane, one would expect an increase in the area experiencing significant sensor-induced LST effects. This is especially true for areas having hot spot conditions. However, these extreme geometric conditions are rarely met in the year 2000 because the sun is too low in the sky—the solar zenith angle exceeds the view zenith angle.

The effects are illustrated for the forest site (Fig. 15). For this date, the correlation between LST and sunlit crown is not obvious, and no hot spot exists. Indeed, for year 2000, we found few significant correlations between LST and the projected fractions over the different landcover types (dense or sparse). However, for each test area studied, we observed a decrease in the variability of LST with view zenith angle. This likely results from the convergence of endmember temperatures for measurements taken later in the day (around 16:30; recall Fig. 14). Indeed, when all endmember temperatures are the same, the scene resembles an isotropically emitting surface.

#### V. DISCUSSION

The results above provide strong evidence that AVHRR split-window LST data likely have sensor-induced signals that can equal or exceed the short-term (weeks) variability typically manifested in nature. Since diurnal temperature range may be strongly correlated with water stress, some drought indexes may be particularly vulnerable to this extra noise. The geometric sampling biases with season unfortunately coincide with the continent's wet-dry seasonality and rainfall's impact on vegetation foliage. Specifically, the northern part of the continent experiences its wet season, when vegetation foliage is maximized, in May–July when AVHRR samples along the principal plane. Since solar insolation and tree crown shadowing is greatest at that time, the likely changes in endmember fractions along the principal plane and the differences in endmember temperatures are greatest. The consolation is that the opposite end of the continent has minimal overstory foliage and endmember temperature variance where the AVHRR samples in the perpendicular plane.

Clearly, we required many assumptions in our study. For example, we ignored topography, assumed only four primary endmembers, and assumed laboratory emissivity data are representative of large natural areas. We also ignored small inland water bodies (e.g., rivers), human settlements, and assumed homogeneity (or well-mixed aggregations) over 8-km pixels. We also modeled maximum leaf area index conditions only. In theory, in the dry season when leaf area index tends to decrease, the shadowing would be less prominent, and the endmember temperatures differences would decrease. We relied extensively on the land cover and continuous fields satellite products, and we widely extrapolated site-level vegetation structural characteristics from the literature [30].

The use of a pure geometric projection approach to estimate the upward thermal fluxes neglects the vertical profile of temperatures in a 3-D surface. In reality, the infrared radiance observed by a sensor represents an integration of radiative fluxes that originate from leaves at different levels in the canopy, soil, and atmosphere, all of which possibly being at different temperatures [40]. In addition, multiple scattering within the canopy, and to a lesser extent in the atmosphere, also impacts the observed temperature of a surface. We also assume that the split-window algorithm corrects for all atmospheric effects. Finally, our scatter plots of LST versus view zenith angle [e.g., Fig. 11(a)] consist of data for different parts of the AVHRR swath. Therefore, their observation time varies slightly with each sample. We assume LST differences from this effect, as well as those due to day-to-day meteorological changes, are small relative to those from geometric effects.

Nevertheless, we believe our assumptions are reasonable for a continental analysis. The implications of these findings could be significant. Split-window methods are common such that directional effects may also be impacting MODIS and other LST products. New sensors (e.g., the Visible Infrared Imager/Radiometer Suite on the National Polar-orbiting Operational Environmental Satellite System (NPOESS) Preparatory Project and NPOESS satellites) will extend the split-window LST record to at least year 2025. Still, finding evidence of directional effects is only the first step. A strong effort must follow to fully characterize the behavior for different geographical, seasonal, meteorological, topographical, and vegetation structural conditions. Ultimately, of course, an operational correction is desirable such that a normalized LST climate data product (global time series spanning AVHRR history) can be produced. This last step will clearly be a major challenge. First, normalization to a nadir viewing geometry (independent of relative azimuth angle) will likely require information about the instantaneous overstory and understory or background temperatures. Transpirative cooling variability with rooting depth, soil moisture, and wind speed makes this nearly intractable *a priori*. Thus, this problem may require coupling of an AVHRR LST algorithm to an energy budget model that assimilates detailed meteorological data (cloudiness, precipitation, surface winds and air temperature, vapor pressure deficit, aerosol optical depth, etc.). Statistical-empirical view angle corrections may provide a second approach.

Solar angle normalization presents different challenges. As noted, in addition to sample time differences from orbital drift,

wide field-of-view sensors scan a range of local times over its wide swath. Due of thermal inertia effects, solar zenith angle and time-of-day may not be well correlated, even for a given location. Therefore, perfect knowledge of projected endmember fractions and a dynamic model of endmember temperature change with time may be needed.

Although we have only considered split-window algorithms in our analysis, this approach is the most commonly used in research and applications. It should be noted that the EOS MODIS LST algorithm includes both a split-window algorithm [41] and a unique “day–night” algorithm [42] that simultaneously uses day/night pairs of MODIS data. We are currently investigating the directional effects in these products.

## VI. CONCLUSION

The objective of the present study was to develop a daily (day and night) AVHRR LST dataset for the years 1995 to 2000, and to determine if it contained systematic biases as a result of the varying sun-view geometry characteristics of the observing system. Although theoretical and local “point-scale” ground studies show evidence of angular dependency in LST observations, we are not aware of any prior studies that demonstrate that LST data, collected by wide-field-of-view sensors such as AVHRR, are systematically affected by sun-view geometry of the observing system.

Our hypothesis was based on the assumption that the radiance received by the sensor is a weighted average of the radiance emitted from scene endmembers. The weighting factors depend on the projected fraction of each endmember of the sensor. We expected to detect an induced, deterministic component of the LST variability that is mainly a function of the geometry variability of the observation, in addition to the natural variability of the surface temperature. We have demonstrated that there is a bias in the NOAA-14 AVHRR LST dataset that results from the orbit and sensor characteristics. This bias is not uniform in time or in space and responds not only to the latitudinal and seasonal patterns of the AVHRR geometry, but also to the differences in tree cover density. Our results suggest that, given the orbital drift of NOAA-14, the angular effects on LST decrease with time past launch. Although sensors degrade with age, the reduction in sensor-induced biases in afternoon AVHRR LST with time may provide some compensation.

Our results highlight the need to account for this artifact in the AVHRR LST data. A methodology could be developed to normalize the data to a common illumination and observation geometries and, therefore, remove the angular dependency that currently exists in the AVHRR thermal retrievals. This is the subject of current work and will be reported at a later date.

## ACKNOWLEDGMENT

The authors thank C. Justice, M. Hansen, R. Defries, W. Ni, L. Giglio, and N. Saleous for their models, data, and advice.

## REFERENCES

- [1] P. J. Sellers, F. G. Hall, G. Asrar, D. E. Strebel, and R. E. Murphy, “An overview of the First International Satellite Land Surface Climatology Project (ISLSCP) Field Experiment (FIFE),” *J. Geophys. Res.*, vol. 97, pp. 18 345–18 371, 1992.

- [2] R. Nemani, L. Pierce, and S. Running, "Developing satellite-derived estimates of surface moisture status," *J. Appl. Meteorol.*, vol. 32, pp. 548–557, 1993.
- [3] R. E. Dickinson, "Water and energy exchange," in *Remote Sensing of Biospheric Functioning*, R. J. Hobbs and H. A. Mooney, Eds. Berlin, Germany: Springer-Verlag, pp. 105–133.
- [4] R. D. Jackson, S. B. Idso, R. J. Reginato, and P. J. Pinter, Jr., "Canopy temperature as a crop water stress indicator," *Water Resour. Res.*, vol. 17, no. 4, pp. 1133–1138, 1981.
- [5] T. C. Carlson, "Regional-scale estimates of surface moisture availability and thermal inertia using remote thermal measurements," *Remote Sens. Rev.*, vol. 1, pp. 197–247, 1986.
- [6] S. W. Running, R. Nemani, J. M. Glassy, and P. E. Thornton, "MODIS daily photosynthesis (PSN) and annual net primary production (NPP) product (MOD17)," NASA, Greenbelt, MD, Algorithm Theoretical Basis Doc. Ver. 3.0, Apr. 29, 1999.
- [7] M. Jin and R. E. Treadon, "Correcting orbit drift effect on AVHRR land surface skin temperature measurements," *Int. J. Remote Sens.*, vol. 24, no. 22, pp. 4543–4558, 2003.
- [8] W. P. Kustas and J. M. Norman, "Use of remote sensing for evapotranspiration monitoring over land surfaces," *Hydrol. Sci.*, vol. 41, no. 4, pp. 495–515, 1996.
- [9] J. C. Price, "Timing of NOAA afternoon passes," *Int. J. Remote Sens.*, vol. 12, no. 1, pp. 193–198, 1991.
- [10] G. G. Gutman, "On the monitoring of land surface temperature with the NOAA/AVHRR: Removing the effect of satellite orbit drift," *Int. J. Remote Sens.*, vol. 20, no. 17, pp. 3407–3413, 1999.
- [11] D. S. Kimes and J. A. Kirchner, "Directional radiometric measurements of row-crop temperatures," *Int. J. Remote Sens.*, vol. 4, no. 2, pp. 299–311, 1983.
- [12] J. P. Lagourde, Y. H. Kerr, and Y. Brunet, "An experimental study of angular effects on surface temperature for various plant canopies and bare soils," *Agricult. Forest Meteorol.*, vol. 77, pp. 167–190, 1995.
- [13] F. Jacob, X. F. Gu, J. F. Hanocq, N. Tallet, and F. Baret, "Atmospheric corrections of single broadband channel and multidirectional airborne thermal infrared data: Application to the ReSeDA experiment," *Int. J. Remote Sens.*, vol. 24, no. 16, pp. 3269–3290, Aug. 2003.
- [14] M. Minenti, L. Jia, Z.-L. Li, V. Djepa, J. Wang, M. P. Stoll, Z. Su, and M. Rast, "Estimation of soil and vegetation temperatures with multiangular thermal infrared observations: IMGRASS, HEIFE, and SGP 1997 experiments," *J. Geophys. Res.*, vol. 106, no. D11, pp. 11997–12010, 2001.
- [15] A. Chehbouni, Y. Nouvellon, J.-P. Lhomme, C. Watts, G. Boulet, Y. Kerr, M. S. Moran, and D. C. Goodrich, "Estimation of surface sensible heat flux using dual angle observations of radiative temperature," *Agricult. Forest Meteorol.*, vol. 108, pp. 55–65, 2001.
- [16] J. A. Sobrino, Z.-L. Li, M. P. Stoll, and F. Becker, "Multi-channel and multi-angle algorithms for estimating sea and land surface temperature with ATSR data," *Int. J. Remote Sens.*, vol. 17, no. 11, pp. 2089–2224, 1996.
- [17] J. V. Vogt *et al.*, "Land surface temperature retrieval from NOAA AVHRR data," in *Advances in the Use of NOAA-AVHRR Data for Land Application*, G. D'Souza *et al.*, Eds. Dordrecht, The Netherlands: Kluwer, 1996, pp. 125–151.
- [18] X. W. Li, J. D. Wang, and A. H. Strahler, "Scale effects and scaling-up by geometric-optical model," *Sci. China*, ser. Series E 43 Suppl. S, pp. 17–22, Dec. 2000.
- [19] J. A. Smith and J. R. Ballard, Jr., "Preliminary calculation of TIR canopy hot spot and implications for earth radiation budget," in *Proc. IGARSS*, Honolulu, HI, July 24–28, 2000.
- [20] J. M. Norman and F. Becker, "Terminology in thermal infrared remote sensing of natural surfaces," *Remote Sens. Rev.*, vol. 12, pp. 159–173, 1995.
- [21] F. Becker and Z.-L. Li, "Surface temperature and emissivity at various scales: Definition, measurement, and related problems," *Remote Sens. Rev.*, vol. 12, pp. 225–253, 1995.
- [22] D. S. Kimes, "Effects of vegetation canopy structure on remotely sensed canopy temperature," *Remote Sens. Environ.*, vol. 10, pp. 165–174, 1980.
- [23] M. Owe and A. A. Van de Griend, "Ground-based measurements of surface temperature and thermal emissivity," *Adv. Space Res.*, vol. 14, no. 3, pp. 45–48, 1994.
- [24] D. S. Kimes and J. A. Kirchner, "Directional radiometric measurements of row-crop temperatures," *Int. J. Remote Sens.*, vol. 4, no. 2, pp. 299–311, 1983.
- [25] R. D. Jackson, R. J. Reginato, and S. B. Idso, "Wheat canopy temperature: A practical tool for evaluating water requirements," *Water Resour. Res.*, vol. 13, pp. 651–656, 1977.
- [26] J. A. Sobrino and V. Caselles, "Thermal infrared radiance model for interpreting the directional radiometric temperature of a vegetated surface," *Remote Sens. Environ.*, vol. 33, pp. 193–199.
- [27] W. Ni, X. Li, C. E. Woodcock, M. R. Caetano, and A. H. Strahler, "An analytical hybrid GORT model for bidirectional reflectance over discontinuous canopies," *IEEE Trans. Geosci. Remote Sensing*, vol. 37, pp. 987–999, Mar. 1999.
- [28] A. C. Pinheiro and J. L. Privette, "African vegetation structural parameters derived from 8 km AVHRR land classifications," *Remote Sens. Environ.*, submitted for publication.
- [29] M. C. Hansen, R. S. DeFries, J. R. G. Townshend, and R. Sohlberg, "Global land cover classification at 1 km spatial resolution using a classification tree approach," *Int. J. Remote Sens.*, vol. 21, no. 6, pp. 1331–1364, 2000.
- [30] F. White, "The vegetation of Africa, a descriptive memoir to accompany the UNESCO/AETFAT/UNSO vegetation map of Africa," *Nat. Resour. Res.*, vol. 20, pp. 1–356, 1983.
- [31] R. S. DeFries, M. C. Hassen, and J. R. G. Townshend, "Global continuous fields of vegetation characteristics: A linear mixture model applied to multi-year 8 km AVHRR data," *Int. J. Remote Sens.*, vol. 21, no. 6, pp. 1389–1414, 2000.
- [32] A. C. Pinheiro, J. L. Privette, and P. Guillevis, "Directional variability in land surface temperature in an African savanna," *IEEE Trans. Geosci. Remote Sensing*, submitted for publication.
- [33] C. J. Tucker, W. E. Newcomb, and H. E. Dregne, "Improved data sets for determination of desert spatial extent," *Int. J. Remote Sens.*, vol. 15, pp. 3519–3545.
- [34] L. L. Stowe, P. A. Davis, and E. P. McClain, "Scientific basis and initial evaluation of the CLAVR-1 global clear/cloud classification algorithm for the advanced very high resolution radiometer," *J. Atmos. Oceanic Technol.*, vol. 16, pp. 656–681, 1998.
- [35] C. Ulivieri, M. M. Castronuovo, R. Francioni, and A. Cardillo, "A split window algorithm for estimating land surface temperature from satellites," *Adv. Space Res.*, vol. 14, no. 3, pp. 59–65, 1994.
- [36] D. P. Vazquez, F. J. O. Reyes, and L. A. Arboledas, "A comparative study of algorithms for estimation of land surface temperature from AVHRR," *Remote Sens. Environ.*, vol. 62, pp. 215–222, 1997.
- [37] A. C. Wilber, D. P. Kratz, and S. K. Gupta, "Surface emissivity maps for use in satellite retrievals of longwave radiation," Langley Res. Center, Hampton, VA, NASA/TP-1999-209362, 1999.
- [38] FAO-UNESCO, *Soils of the World*. New York: Elsevier, 1987.
- [39] X. W. Li, "A hybrid geometric optical-radiative transfer approach for modeling albedo and directional reflectance of discontinuous canopies," *IEEE Trans. Geosci. Remote Sensing*, vol. 33, pp. 460–480, Mar. 1995.
- [40] P. Guillevis, J. P. Gastellu-Etchegorry, J. Demarty, and L. Prevot, "Thermal infrared radiative transfer within three-dimensional vegetation covers," *J. Geophys. Res.—Atmos.*, vol. 108(D8), no. 4248, Apr. 2003.
- [41] Z. M. Wan and J. Dozier, "A generalized split-window algorithm for retrieving land-surface temperature from space," *IEEE Trans. Geosci. Remote Sensing*, vol. 34, pp. 892–905, July 1996.
- [42] Z. M. Wan and Z. L. Li, "A physics-based algorithm for retrieving land-surface emissivity and temperature from EOS/MODIS data," *IEEE Trans. Geosci. Remote Sensing*, vol. 35, pp. 980–996, July 1997.
- [43] J. L. Privette, C. Fowler, G. A. Wick, D. Baldwin, and W. J. Emery, "Effects of orbital drift on advanced very high resolution radiometer products: Normalized difference vegetation index and sea surface temperature," *Remote Sens. Environ.*, vol. 53, pp. 164–171, 1995.



**Ana C. T. Pinheiro** received the B.S. degree in environmental engineering from the New University of Lisbon, Lisbon, Portugal, in 1996, the M.Eng. degree in civil and environmental engineering from the Massachusetts Institute of Technology, Cambridge, in 1998, and the Ph.D. degree in environmental engineering from the New University of Lisbon, in 2003. She conducted her doctoral research as a Visiting Scientist in the Biospheric Sciences Branch, National Aeronautics and Space Administration (NASA) Goddard Space Flight Center (GSFC), Greenbelt, MD.

She is currently a National Research Council Postdoctoral Researcher at the Hydrological Sciences Branch, NASA GSFC.



**Jeffrey L. Privette** received the Ph.D. degree in aerospace engineering sciences from the University of Colorado, Boulder, in 1994.

He is currently Acting Project Scientist for the NPOESS Preparatory Project. He has been with the Biospheric Sciences Branch, National Aeronautics and Space Administration, Goddard Space Flight Center, Greenbelt, MD, since 1996. His research has focused on the retrieval of land biophysical parameters via solar-reflected and thermal infrared remote sensing. He has held leadership positions in

SAFARI 2000, the MODIS Validation Program, the CEOS Working Group for Calibration and Validation (WGCV), and the NPP/NPOESS programs.



**Compton J. Tucker** received the B.S. degree in biology, in 1969, and the M.S. degree, in 1973, and the Ph.D. degree, in 1975, all from Colorado State University, Fort Collins.

He is currently a Senior Earth Scientist with the Laboratory for Terrestrial Physics, National Aeronautics and Space Administration, Goddard Space Flight Center, Greenbelt, MD. He is also an Adjunct Professor with the University of Maryland, College Park.



**Robert Mahoney** received the B.A. degree in meteorology and the M.S. degree in atmospheric science, in 1978 and 1980, respectively, both from the University of California, Los Angeles.

He is currently with the NPOES Team at Northrop Grumman Space Technology, El Segundo, CA. Between 1982 and 2004, he was a Support Contractor for the National Aeronautics and Space Administration (NASA), Goddard Space Flight Center (GSFC), NASA/GSFC, Greenbelt, MD, with Global Science and Technology, Inc. (1995–2004), and with Science

Systems and Applications Inc. (1982–1995). While with GSFC, he provided support on projects ranging from global remote sensing of vegetation, MODIS instrument calibration, retrieval of anthropogenic aerosol optical thickness, to development of environmental and human health applications using remotely sensed satellite data.